Acoustic plasmons and conducting carriers in hole-doped cuprate superconductors

A. Singh, H. Y. Huang, Christopher Lane, J. H. Li, J. Okamoto, S. Komiya, Robert S. Markiewicz, Arun Bansil, T. K. Lee, A. Fujimori, C. T. Chen, and D. J. Huang

Phys. Rev. B **105**, 235105 — Published 9 June 2022

DOI: 10.1103/PhysRevB.105.235105

Acoustic plasmons and conducting carriers in hole-doped cuprate superconductors

A. Singh,[1] H. Y. Huang,[1] Christopher Lane,[2,3] J. H. Li,[4] J. Okamoto,[1] S. Komiya,[5] Robert S. Markiewicz,[6] Arun Bansil,[6] T. K. Lee,[7,8] A. Fujimori,[9,1] C. T. Chen,[1] and D. J. Huang[1,4,*]

[1] *National Synchrotron Radiation Research Center, Hsinchu 30076, Taiwan*
[2] *Theoretical Division, Los Alamos National Laboratory, Los Alamos, New Mexico 87545, USA*
[3] *Center for Integrated Nanotechnologies, Los Alamos National Laboratory, Los Alamos, New Mexico 87545, USA*
[4] *Department of Physics, National Tsing Hua University, Hsinchu 30013, Taiwan*
[5] *Central Research Institute of Electric Power Industry, Yokosuka, Kanagawa, 240-0196, Japan*
[6] *Physics Department, Northeastern University, Boston, Massachusetts 02115, USA*
[7] *Institute of Physics, Academia Sinica, Taipei 11529, Taiwan*
[8] *Department of Physics, National Sun Yat-sen University, Kaohsiung, 80424, Taiwan*
[9] *Department of Applied Physics, Waseda University, Shinjuku-ku, Tokyo 169-8555, Japan.*

(Dated: May 9, 2022)

The layered crystal structures of cuprates enable collective charge excitations fundamentally different from those of three-dimensional metals. Acoustic plasmons have been observed in electron-doped cuprates by resonant inelastic X-ray scattering (RIXS); in contrast, the characteristics of acoustic plasmons in hole-doped cuprates are under debate, despite extensive measurements. This contrast led us to investigate the charge excitations of hole-doped cuprate $La_{2-x}Sr_xCuO_4$. Here we present incident-energy-dependent RIXS measurements and calculations of collective charge response via the loss function to reconcile the issues above. Our results provide evidence for the acoustic plasmons of Zhang-Rice singlet (ZRS), which has a character of the Cu $3d_{x^2-y^2}$ strongly hybridized with the O $2p$ orbitals; the metallic behavior is implied to result from the movement of ZRS rather than the simple hopping of O $2p$ holes.

I. INTRODUCTION

The superconductivity of cuprates, which has been a mystery ever since its discovery decades ago, is created through doping electrons or holes into a Mott insulator[1,2]. There exists an inherent electron-hole asymmetry in cuprates[3,4]. The antiferromagnetic phase of electron-doped cuprates persists at higher doping concentrations, and its superconductivity is more difficult to achieve. Electron correlations in electron-doped cuprates appear weaker than those of hole-doped compounds. Measurements of resonant inelastic X-ray scattering (RIXS) reveal acoustic plasmons in electron-doped cuprates[5,6], showing the characteristic of conduction electrons of a layered system as shown in Fig. 1(a) in the presence of a long-range Coulomb interaction[7,8]. Acoustic plasmons of hole-doped cuprates, however, were not observed in measurements of Cu L-edge RIXS[9–14]. Although optical plasmons with a quadratic dispersion appear in measurements of electron energy loss spectroscopy (EELS), acoustic plasmons of cuprates were not detected in EELS measurements[15–19]. Acoustic plasmons of cuprates were also not observed in other studies such as optical spectroscopy, including reflectance and ellipsometry measurements[20–24], which is limited to nearly zero momentum transfer. Interestingly, recent O K-edge RIXS results showed the presence of acoustic plasmons in hole-doped cuprates[25].

The conducting carriers are hallmarks of hole-doped cuprates, but their nature remains elusive. Upon doping, the low-energy excitations in the optical conductivity of $La_{2-x}Sr_xCuO_4$ (LSCO) are much enhanced[21]; the Hall coefficient R_H of LSCO is much smaller than what is expected from the contribution of doped holes[26], i.e., $R_H \ll \frac{1}{n_p e}$, where n_p is the hole density and e is the magnitude of electron charge. Early photoemission studies on superconducting cuprates indicated that the parent compound is a charge-transfer insulator, which led to a conjecture that doped holes are oxygen p-like[27]. Theoretically, doped holes are assumed to enter p orbitals of an O atom between two Cu atoms, i.e., the Emery model[28], or of four oxygen atoms surrounding one Cu atom to form a spin singlet termed a Zhang-Rice singlet (ZRS)[29], as illustrated in Fig. 1(b). O K-edge

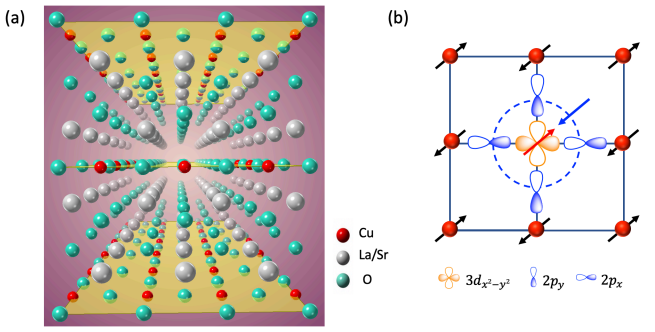

FIG. 1. (a) Crystal structure of LSCO. The stacked CuO_2 layers are highlighted in yellow. (b) Cartoon illustration of a ZRS in the CuO_2 plane. It is a two-hole state formed by a Cu $d_{x^2-y^2}$ hole hybridized with an O $2p_{x,y}$ hole distributed over the surrounding ligands in an antiparallel spin configuration. The singlet moves through the lattice of Cu^{2+} ions in a way similar to that of a mobile hole in the CuO_2 plane. The arrows on Cu^{2+} indicate the antiferromagnetic structure of the lattice.

X-ray absorption[30] and resonant elastic scattering[31] indeed provided experimental evidence for O $2p$ holes. The RIXS results also concluded that the acoustic plasmons are predominantly associated with the O sites through a strong $2p$ character[25]. In contrast, photoemission intensity at the Fermi level showed no resonant enhancement at the O K-edge[32]. Many angle-resolved photoemission data[33] have been interpreted based on band structures in the local density approximation, which predict that Cu d and oxygen p characters are about equally mixed at the Fermi level. In addition, theoretical calculations using the three-band Hubbard model[34] reveal that the ZRS band of hole-doped cuprates is composed of a comparable amount of O $2p$ and Cu $3d_{x^2-y^2}$.

Here we report measurements of incident-energy-dependent O K-edge RIXS to investigate the nature of the conducting carriers of superconducting LSCO with the doping concentration $x = 0.12$. The remainder of this paper is organized as follows: In Section II, we present the experimental technique RIXS and the calculation details. The RIXS results and their comparison with the calculated loss function are discussed in Section III, followed by a conclusion section.

II. METHODS

A. RIXS measurements

The LSCO single crystal was grown by the traveling-solvent floating zone method[35,36]. After growth, the crystals were annealed appropriately to remove oxygen defects. The oxygen content was tuned to be 4.000±0.001 following Ref. [37]. The stoichiometry $x = 0.12$ was determined from an inductively-coupled-plasma atomic-emission spectrometric analysis. The sample's transition temperature T_C of superconductivity was 30 K. See Ref. [35] for the crystal growth and characterization. Based on the above information and the previously published characterizations of LSCO[37,38], our crystal was estimated to have lattice constants $a = b = 3.77$ Å and $c = 13.22$ Å.

We conducted O K-edge RIXS measurements using the AGM-AGS spectrometer of beamline 41A at Taiwan Photon Source. This RIXS beamline has been constructed based on the energy compensation principle of grating dispersion. The instrumental energy resolution defined as the full width at half maximum (FWHM) was ~ 20 meV for all RIXS measurements with the monochromator exit slit set to 100 μm. See Ref. [39] for more details of the beamline. Figure 2(a) shows the scattering geometry of our RIXS measurements. The crystallographic axes of the LSCO crystal were precisely aligned with X-ray diffraction using a unique holder with tilting adjustment. Prior to RIXS measurements, the LSCO sample was cleaved in air and then mounted on a 3-axis in-vacuum manipulator through a load-lock system. X-ray absorption spectra were measured using a photodiode in the fluorescence yield mode. The resonant conditions were achieved by tuning the energy of the incident X-ray to the Zhang-Rice singlet (ZRS) about 528.3 eV or the upper Hubbard band (UHB)[30,40]. RIXS measurements were recorded with σ-polarized incident X-rays and normalized to the fluorescence intensity for various in-plane wave-vector changes. The sample was cooled to 23 K with liquid helium.

B. Theoretical calculations

In a RIXS process, a photon scatters resonantly to another state, leaving behind an electron-hole excitation of well-defined momentum $\mathbf{q}$ and energy ω. The general expression for the K-edge RIXS intensity[41,42] can be expressed as[43]

$$I_{RIXS}(\mathbf{q},\omega,\omega_i) = (2\pi)^3 N \left|w(\omega,\omega_i)\right|^2 \frac{\hat{v}(\mathbf{q})^2}{v(\mathbf{q})} L(\mathbf{q},\omega), \quad (1)$$

where $w(\omega,\omega_i)$ is the energy dependent matrix element, $\hat{v}(\mathbf{q})$ ($v(\mathbf{q})$) is the interaction energy of between electron-hole (electron-electron), and $L(\mathbf{q},\omega)$ is the loss function in the charge channel

$$\mathrm{Im}\left[-\varepsilon_{00}^{-1}\right], \quad (2)$$

with ε_{00}^{-1} being the inverse dielectric function. Therefore, peaks of K-edge RIXS intensity are directly proportional to transitions in the loss function, which mark the presence of collective charge modes, or plasmons[44]. To construct the inverse dielectric function we follow Ref. [45], where it is defined as

$$\varepsilon_{IJ}^{-1} = \left[\delta_{NL} - v_{NK} P_{KL}\right]_{IJ}^{-1}. \quad (3)$$

$I(J) = 0$ index the charge components, while $I(J) \in \{x, y, z\}$ denote the various spin channels. By assuming a non-interacting ground state and taking the vertex to be the identity, ε_{IJ}^{-1} is the random-phase-approximation (RPA) dielectric function and P_{KL} the Lindhard polarizability. Since the electronic dispersion is local-density-approximation-like for $x = 0.12$ [Ref. 46], we use the single-band electronic dispersion ε_k as defined in Refs. [47,47] with the hopping parameters given in Table I.

TABLE I. Tight-binding hopping parameters (in meV) used in this study.

t	t'	t''	t'''
312.5	-31.25	25.0	68.75

To generate acoustic plasmons we must go beyond the usual Hubbard limiting case and consider the full long-range Coulomb interaction. Moreover, the treatment of the long-range Coulomb interaction for the correlated electronic system in a layered structure requires

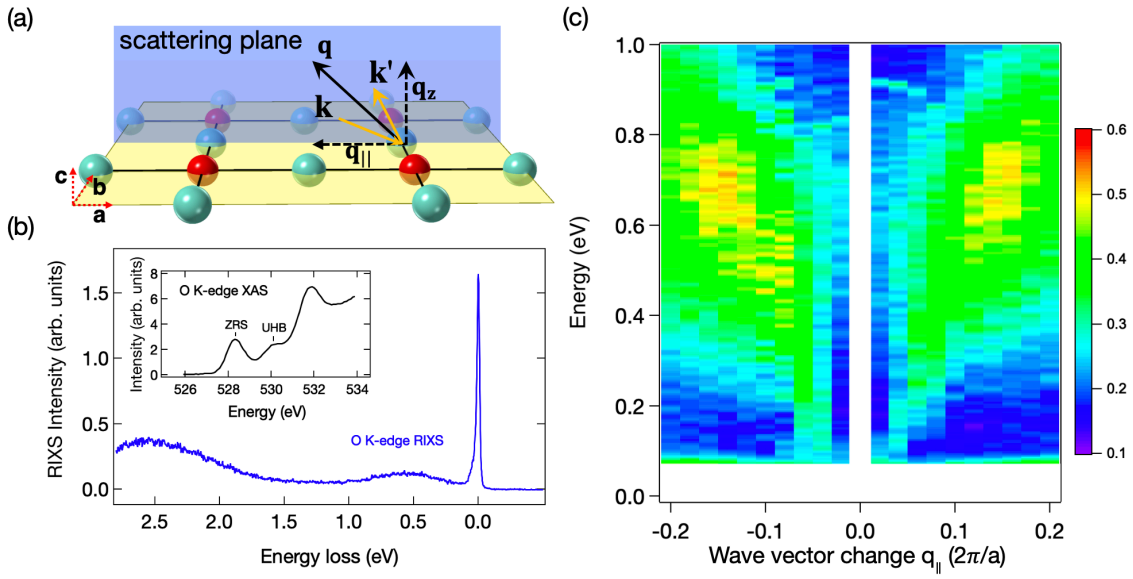

FIG. 2. (a) Scattering geometry of RIXS measurements. The CuO_2 plane is perpendicular to the scattering plane defined by $\mathbf{k}$ and $\mathbf{k}'$, which are the wave vectors of the incident and scattered X-rays, respectively. The projection of the wave vector change onto the CuO_2 plane, $\mathbf{q}_{\parallel}$, is parallel to the antinodal direction. (b) O K-edge RIXS spectrum of LSCO. This spectrum was recorded for a sample at temperature 23 K and with $\mathbf{q}_{\parallel} = (0.1, 0)$ and $q_z = 0.7$. The total energy resolution of the RIXS monochromator and spectrometer was 20 meV. The incident photon energy was set to the absorption at the ZRS resonance. Inset: XAS spectrum recorded through a fluorescence yield scheme. (c) RIXS intensity distribution map of LSCO in the energy-momentum space. The wave-vector change $\mathbf{q}$ is decomposed into an in-plane wave-vector change $\mathbf{q}_{\parallel}$ that varies along the antinodal direction and q_z is fixed to 0.7. RIXS spectra were recorded with incident X-rays tuned to the ZRS resonance.

some care. We model $v(r)$ as $\sum_i \bar{v}(\mathbf{R}_i)\delta(r - \mathbf{R}_i)$, so that $v(\mathbf{q}) = \sum_i \bar{v}(\mathbf{R}_i)\exp(-i\mathbf{q}\cdot\mathbf{R}_i)$. $\bar{v}(\mathbf{R}_i)$ is taken to be an on-site Hubbard $U = 2$ eV (Ref. [49]) for $\mathbf{R}_i = 0$ and a screened Coulomb interaction contribution $\bar{v}(\mathbf{R}_i) = e^2/(\varepsilon_0\mathbf{R}_i)$ for $\mathbf{R}_i \neq 0$, using a background dielectric constant $\varepsilon_0 = 6$. To recover the correct $q \to 0$ limit of $v(\mathbf{q})$ we range separate $v(\mathbf{r})$ into short-range (SR) and long-range (LR) pieces. For the short-range interactions where r less than or equal to a cut-off L we sum the contributions of all in-plane Cu terms. We approximate the remaining long-range component ($r > L$) by a continuum. Then after summing over the interplane contribution we arrive at the following expression for $v(\mathbf{q})$[43,50],

$$v(\mathbf{q}) = v_{2d}^{SR}(\mathbf{q}) + v_{2d}^{LR}(\mathbf{q}) + v_z(\mathbf{q}), \tag{4}$$

where

$$v_{2d}^{SR}(\mathbf{q}) = U + \sum_{i\neq 0}^{L} \frac{e^2}{\varepsilon_0 R_i} e^{-i\mathbf{q}\cdot\mathbf{R}_i}, \tag{5a}$$

$$v_{2d}^{LR}(\mathbf{q}) = \frac{2\pi e^2}{\varepsilon_0 a^2 q_{\parallel}} \left[1 - q_{\parallel}L J_0(q_{\parallel}L)\frac{\pi q_{\parallel}L}{2}\left(J_0(q_{\parallel}L)H_1(q_{\parallel}L) - J_1(q_{\parallel}L)H_0(q_{\parallel}L)\right)\right], \tag{5b}$$

$$v_z(\mathbf{q}) = \frac{2\pi e^2}{\varepsilon_0 a^2 q_{\parallel}} \left[\frac{\cos(q_z l) - e^{-q_{\parallel}l}}{\cosh(q_{\parallel}l) - \cos(q_z l)}\right]. \tag{5c}$$

a and $l = c/2$ are the in-plane lattice parameter and distance between adjacent CuO_2 planes in La_2CuO_4[51,52], respectively, J_i (H_i) are the Bessel (Struve) functions, and the short-range cut-off L is $500a$. Then by inserting $v(q)$ in Eq. (3) we obtain the loss function.

III. RESULTS AND DISCUSSIONS

A. RIXS results

LSCO has a quasi-two-dimensional (2D) crystal structure with stacked CuO_2 layers. This system is theoret-

ically expected to exhibit acoustic plasmons[8]. Whereas optical spectroscopy is limited to measurements of nearly zero momentum transfer, RIXS can probe the dispersion of acoustic plasmons in cuprates[5,6,25]. However, the conclusion drawn from O K-edge RIXS results[25] is inconsistent with EELS results[18,19]. Figure 2(b) plots a typical RIXS spectrum of hole-doped cuprate LSCO with the incident photon energy set to the ZRS resonance in XAS denoted in the inset. This spectrum includes the following features: elastic scattering, phonon excitations, plasmons, para-bimagnons, d-d excitations, and electron-hole pair excitations. Because of the limited energy resolution of the RIXS spectrometer, the low-energy phonon excitations were not well resolved from the elastic scattering, giving rise to an asymmetric and intense spectral profile near the zero energy loss[53]. Because the O $2p$ bands are strongly hybridized with Cu $3d$, d-d excitations of Cu and the excitonic excitations of ZRS occur in this RIXS spectrum at an energy loss above 1.5 eV; these excitation energies overlap with the energy of resonant fluorescence. Distinct from the Cu L_3-edge RIXS measurements, the O K-edge resonance yields negligible single-magnon excitations but permits us to observe even-order spin excitations. The excitation of para-bimagnons, which are called bimagnons throughout the paper for simplicity, appears in the broad feature at an energy loss centered at about 0.5 eV in LSCO[54,56]. This broad feature might also contain plasmon excitations, depending on the wave-vector change, which is composed of in-plane wave-vector change $\mathbf{q}_\parallel$ and out-of-plane component q_z, i.e., $\mathbf{q} = \mathbf{q}_\parallel + q_z\hat{\mathbf{z}}$; they are expressed in units of $\frac{2\pi}{a}$ and $\frac{2\pi}{c}$ throughout the paper, respectively.

We measured $\mathbf{q}$-dependent spectra on LSCO ($x = 0.12$) to examine acoustic plasmons in hole-doped cuprates. Figure 2(c) maps the distribution of RIXS intensity as a function of in-plane wave-vector change $\mathbf{q}_\parallel$ along the antinodal direction with q_z fixed to 0.7. This measurement method differs from those used in most of previous momentum-resolved RIXS measurements on cuprates in which q_z was not fixed[6,14]. In addition to the quasi-elastic scattering, overall this RIXS intensity map shows a broad feature that shifts toward higher energy with an increasing width as $q_\parallel$ is increased. After scrutinizing the RIXS data with $\mathbf{q}_\parallel$ near the zone centre, we found that the RIXS spectrum of $\mathbf{q}_\parallel = (0.04, 0)$ contains a low-energy narrow feature near 0.14 eV and a broad feature of bimagnon excitation centred at about 0.5 eV, like bimagnons in the undoped compound La_2CuO_4.

B. RIXS data analysis and curve fitting

In the RIXS spectra recorded at the ZRS resonance, the bimagnon energy overlaps closely with the plasmon energy of $q_\parallel$ larger than 0.06. We analyzed the RIXS spectra measured at the ZRS and UHB resonances through a non-linear least-squares curve fitting. Prior to the fitting, spectra were normalized to the incident photon flux and corrected for self-absorption[53,57]. Each of the plasmon, bimagnon and phonon components was fitted with an anti-symmetrized Lorentzian function $f(\omega)$ expressed as

$$f(\omega) = \frac{\gamma}{2\pi}\left[\frac{1}{(\omega-\omega_0)^2+(\gamma/2)^2} - \frac{1}{(\omega+\omega_0)^2+(\gamma/2)^2}\right], \quad (6)$$

where ω_0 is the transition energy and γ is FWHM[5,25]. A cubic background was used to account for the tail contribution of $d-d$ excitation. In addition, we used a Gaussian function for the component of elastic scattering.

First, we fitted the spectrum of in-plane momentum $q_\parallel = 0.02$ with four components: one Gaussian function for elastic scattering with an instrumental energy resolution of 20 meV and three anti-symmetrized Lorentzian functions for bimagnon, plasmon, and phonon of energy between 0.03 and 0.05 eV (Ref. [53]). We used the previously published results[25,54] to limit the bimagnon energy to be larger than 0.4 eV and found that it was a broad peak centered about 0.5 eV. For the fitting of RIXS spectra of other in-plane momenta, the position and FWHM of the bimagnon component were constrained to be close to those obtained from the fit results of $q_\parallel = 0.02$ within ± 0.025 eV and ± 0.15 eV, respectively. The constraints of the bimagnon energy and width in curve fitting may cause some uncertainty about the plasmon dispersion, although the deduced dispersion is similar to that of electron-doped cuprates. The conclusion from RIXS at the ZRS resonance requires further verification because of the spectral contributions of bimagnons. We varied the incident photon energy in the RIXS measurements to the UHB resonance to diminish the spectral weight of the bimagnon. The bimagnon contribution to the RIXS spectra measured at the UHB resonance is nearly negligible, particularly for high $q_\parallel$. Since the UHB is more localized and at about 2 eV higher than the ZRS band, RIXS excitations directly involved with the ZRS resonance are more sensitive to bimagnons than those with the UHB resonance[54]. The $q_\parallel$-dependent widths of acoustic plasmons obtained from the curve fitting results of RIXS data at the UHB resonance justify those from the data measured at the ZRS resonance. See Figs. S1 and S2 in the Supplemental Material[55] for the comparison of

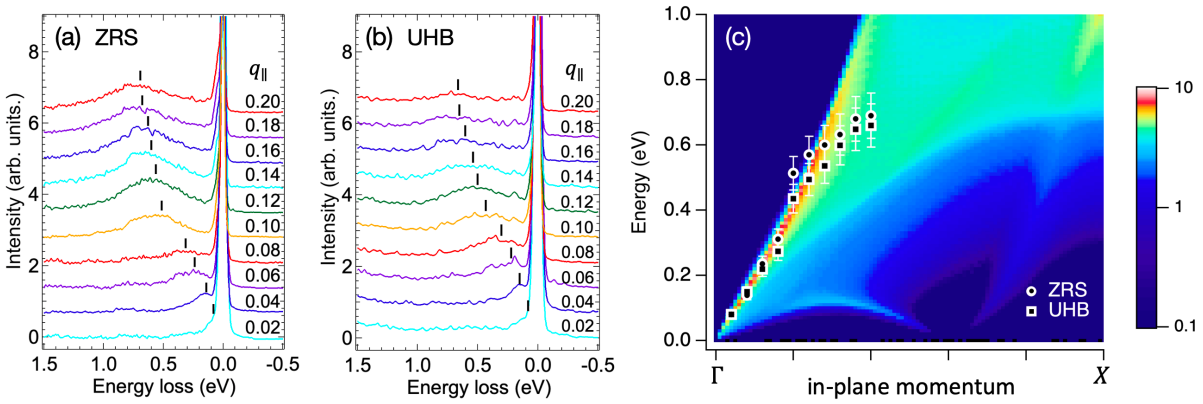

FIG. 3. (a) & (b) Momentum-dependent RIXS spectra of LSCO excited by X-rays of energy tuned to the ZRS and the UHB resonances, respectively. The out-of-plane component q_z was fixed to 0.7. Colour curves in (a) are spectra deduced from Fig. 2(c) after 10-point binomial smoothing and subtraction of the bimagnon component and the background. RIXS spectra shown in (b), which are multiplied by 3 to account for the difference in the cross section between the ZRS and UHB resonances, are plotted without bimagnon and background subtractions. The details of data analysis are presented in the Supplemental Material[55]. Spectra in both (a) and (b) are offset vertically for clarity; vertical ticks indicate the plasmon energies. (c) Theoretically obtained loss function for LSCO with hole-doping $x = 0.12$ along $\Gamma - X$ in the square Brillouin zone with $q_z = 0.7$. Measured plasmon energies of LSCO (circles & squares) deduced from the RIXS spectra shown in (a) and (b) are also plotted for comparison.

the fitted curves with measured data. Table II lists the fitted parameters of our curve-fitting analysis.

Figure 3(a) plots the spectra of various $q_{\parallel}$ after subtraction of the bimagnon and background; it reveals that the energy of the acoustic plasmon monotonically increases from 0.08 eV to 0.69 eV as $q_{\parallel}$ is increased to 0.2. The obtained plasmon dispersion of LSCO is similar to that of electron-doped cuprate $La_{2-x}Ce_xCuO_4$ (LCCO)[5]. Our results indicate that the plasmons of hole-doped cuprates are strongly damped and have a greater spectral width than those of electron-doped cuprates because of stronger electron correlations[4,58]. For example, the plasmon FWHM of LSCO at $q_{\parallel} = 0.1$ and $q_z = 1.0$ is 0.68 eV, whereas that of LCCO is about 0.3 eV. Figure 3(b) plots momentum-dependent RIXS spectra measured with the X-ray energy set to the UHB resonance, in which the excitations are dominated by Cu $3d$ orbitals. As plotted in Figs. 3(a) and 3(b), the plasmon dispersions excited by X-rays tuned to the ZRS and UHB resonances agree with each other, revealing that both O $2p$ and Cu $3d$ orbitals are involved with the acoustic plasmons.

C. Comparison with the loss function

To verify that the observed collective charge dynamics follow the energy dispersion associated with acoustic plasmons, we calculated the collective charge response of the system via the loss function. That is, on incorporating a long-range Coulomb interaction into the one-band parameterization of LSCO (Ref. [43]) with a hole-doping, we calculated $\varepsilon^{-1}(\mathbf{q},\omega)$, in which ε is the dielectric function, and $\mathbf{q}$ contains both in- and out-of-plane momentum transfer components within the RPA. The three-dimensionality was incorporated through inter-plane Coulomb interactions. The loss function was eventually obtained as $-\mathrm{Im}(\varepsilon^{-1})$.

Figure 4 shows the loss function for values of q_z ranging from 0 to 1. For $q_z = 0$, a clear plasmon peak is seen at the zone center near 0.7 eV, in agreement with optical measurements[21]. As $q_{\parallel}$ changes from Γ to X, the plasmon peak disperses to higher energies, eventually entering the particle-hole continuum around $(\pi/2, 0)$, where the peak intensity sharply decreases. As q_z increases, the plasmon energy at Γ decreases, becoming zero for $q_z > 0.04$. Moreover, the plasmon dispersion along $\Gamma - X$ softens, becoming linear for $q_z > 0.3$, ultimately merging with the electron-hole continuum for very large q_z, which dampens out the plasmon peak entirely. The evolution of the plasmon with q_z is in agreement with Ref. [59], confirming that the existence of acoustic plasmons arises from the out-of-phase motion of electrons on adjacent CuO_2 planes. These calculations explain the discrepancy between EELS and RIXS results. For transmission-type EELS, the magnitude of electron momentum is typically larger than $2\pi/c$ by a couple of orders[15–17]. A special scattering geometry is required to pick up the contribution of acoustic plasmons. The refection-type EELS results presented in Ref. [18] and Ref. [19] are dominated by the in-phase motion of electrons on different CuO_2 planes, and they are much less sensitive to acoustic plasmons because the out-of-plane momentum transfers were fixed to $q_z = 20$.

Figure 3(c) plots the calculated loss function for 12% hole-doped LSCO in the paramagnetic phase along the x-axis in the Brillouin zone with $q_z = 0.7$. The measured

TABLE II. Fit results of RIXS spectra recorded at the ZRS and UHB resonances for various in-plan momentum ($q_\parallel$, 0) in units of $2\pi/a$. The energy of plasmon ($\omega_{\rm plasmon}$) and bimagnon ($\omega_{\rm bimag}$) are given in units of eV; their FWHM are expressed by $\gamma_{\rm plasmon}$ and $\gamma_{\rm bigmag}$ in units of eV, respectively.

ZRS					
$q_\parallel$	$\omega_{\rm plasmon}$	$I_{\rm plasmon}$	$\gamma_{\rm plasmon}$	$\omega_{\rm bimag}$	$\gamma_{\rm bimag}$
0.02	0.08 ± 0.01	0.18 ± 0.02	0.23 ±0.05	0.55 ± 0.1	0.8 ± 0.1
0.04	0.14 ± 0.01	0.34 ± 0.04	0.26 ±0.05	0.54 ± 0.1	0.7 ± 0.1
0.06	0.24 ± 0.02	0.35 ± 0.04	0.43 ±0.09	0.55 ± 0.1	0.8 ± 0.1
0.08	0.31 ± 0.02	0.30 ± 0.03	0.56 ±0.12	0.5 ± 0.1	0.8 ± 0.1
0.10	0.51 ± 0.05	0.67 ± 0.07	0.65 ±0.13	0.5 ± 0.1	0.9 ± 0.1
0.12	0.57 ± 0.06	1.10 ± 0.12	0.68 ±0.14	0.5 ± 0.1	0.8 ± 0.1
0.14	0.60 ± 0.06	1.13 ± 0.12	0.70 ±0.15	0.5 ± 0.1	0.8 ± 0.1
0.16	0.63 ± 0.06	1.15 ± 0.13	0.72 ±0.15	0.5 ± 0.1	0.9 ± 0.1
0.18	0.68 ± 0.07	1.03 ± 0.11	0.73 ±0.15	0.5 ± 0.1	0.6 ± 0.1
0.20	0.69 ± 0.07	0.99 ±0.10	0.76 ±0.16	0.5 ± 0.1	0.6 ± 0.1
UHB					
$q_\parallel$	$\omega_{\rm plasmon}$	$I_{\rm plasmon}$	$\gamma_{\rm plasmon}$	$\omega_{\rm bimag}$	$\gamma_{\rm bimag}$
0.02	0.08 ± 0.01	0.07 ± 0.01	0.18 ± 0.04	0.5 ± 0.1	0.6 ± 0.1
0.04	0.15 ± 0.01	0.09 ± 0.01	0.20 ± 0.04	0.5 ± 0.1	0.6 ± 0.1
0.06	0.22 ± 0.02	0.13 ± 0.01	0.35 ± 0.07	0.5 ± 0.1	0.6 ± 0.1
0.08	0.30 ± 0.03	0.24 ± 0.02	0.60 ± 0.12	–	–
0.10	0.44 ± 0.04	0.22 ± 0.02	0.62 ± 0.13	–	–
0.12	0.49 ± 0.05	0.24 ± 0.02	0.63 ± 0.13	–	–
0.14	0.54 ± 0.05	0.22 ± 0.02	0.65 ± 0.13	–	–
0.16	0.60 ± 0.06	0.22 ± 0.02	0.67 ± 0.14	–	–
0.18	0.65 ± 0.06	0.20 ± 0.02	0.69 ± 0.14	–	–
0.20	0.66 ± 0.07	0.18 ± 0.02	0.73 ± 0.15	–	–

plasmon energies of LSCO are also shown for comparison. The dispersion of an acoustic-like plasmon excitation is seen to extend from near zero at the zone center Γ to above 1 eV at X. The slight gap at $q_\parallel = (0, 0)$ is due to the finite interlayer momentum transfer[43,60] in accord with the observed dispersion. The charge fluctuations near the Fermi surface govern the plasmon excitations of small $q_\parallel$. As $q_\parallel$ extends away from the zone center, more incoherent states with decreased lifetime contribute to plasmon excitations, and the width of the plasmon peak increases, consistent with the Landau quasi-particle picture in which the plasmon peak becomes incoherent. As the plasmon enters the particle-hole continuum, the peak broadens, and the slight curve appears to follow the ridge in the particle-hole continuum of the loss function. Consequently, the RIXS spectral width of acoustic plasmons becomes broadened when $q_\parallel$ increases, consistent with the dynamics of the electrons near the Fermi surface. The agreement between our data and theory thus supports the proposal of attributing the zone center mode to acoustic plasmon excitations.

D. 3D nature of acoustic plasmons

Next, we corroborate the acoustic plasmon's three-dimensional (3D) nature originating from the interlayer Coulomb interaction. Figure 5(a) plots the spectra of $\mathbf{q}_\parallel = (0.1, 0)$ with selected q_z. The broad spectral features about 0.5 eV were fitted with two anti-symmetrized Lorentzian functions: one is a q_z-independent component for the bimagnon; the other disperses with the change of q_z. We found that when q_z is altered from 0.6 to 1.0, the energy of this feature decreases by 91 meV for $q_\parallel$ fixed to 0.1, i.e., evidence for the 3D nature of plasmon excitations. Figure 5(b) illustrates the dispersions of the plasmon bands of a layered electron-gas model for the high-T_c cuprates[7]. The plasmon bands are restricted to be in between two boundary branches corresponding to the in-phase motion of electrons on separate planes and the out-of-phase motion on adjacent planes, i.e., $q_z = 0$ and $\frac{\pi}{d}$, respectively, where d is the distance between two adjacent CuO_2 layers and $d = c/2$. Figure 4 shows the loss function for values of q_z ranging from 0 to 1 in units of $2\pi/c$. For $q_z = 0$ [Fig 4 (upper-left panel)] a clear plasmon peak is seen at the zone center near 0.70 eV. As

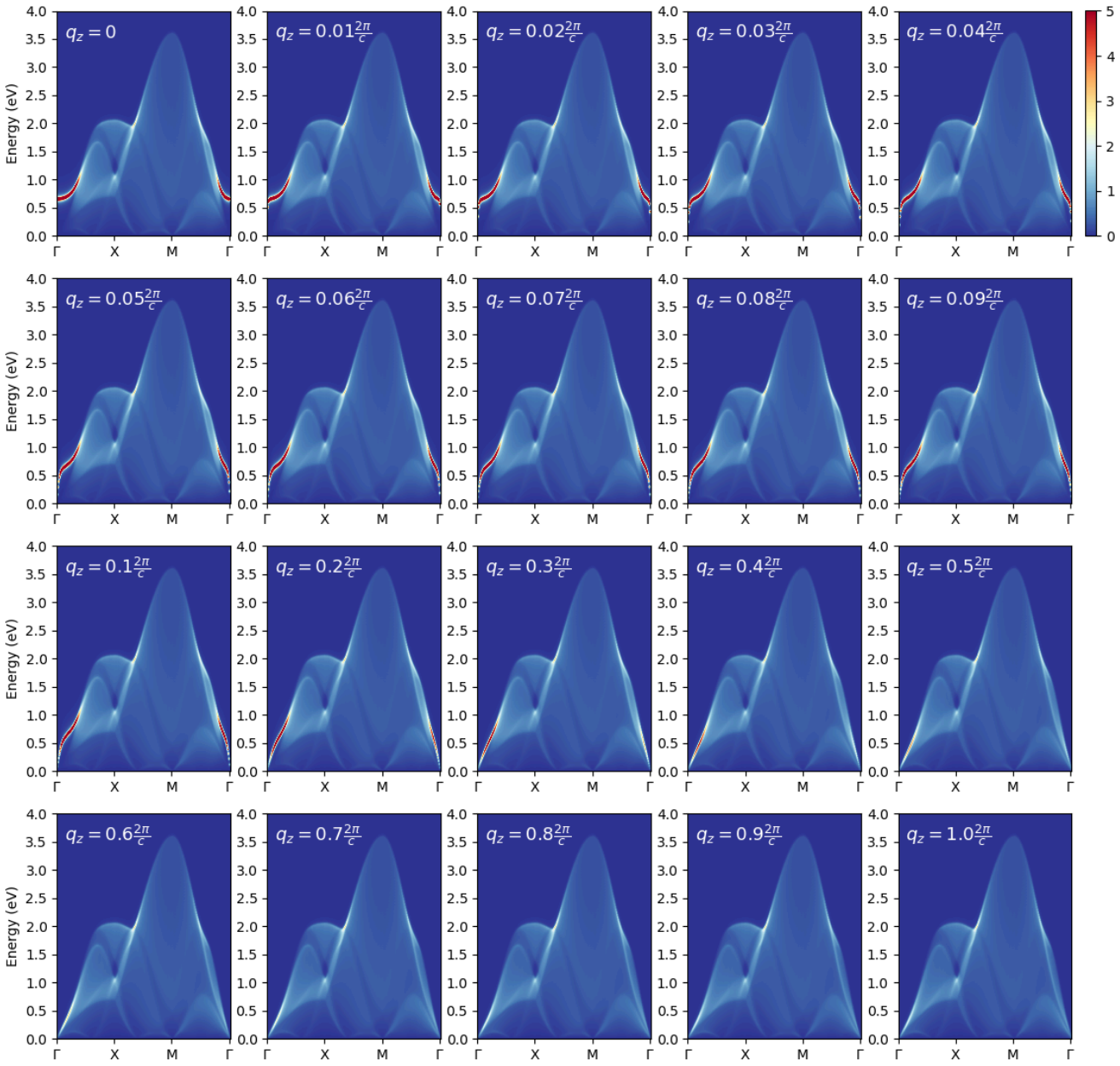

FIG. 4. Calculated loss function along the high-symmetry lines in the square Brillouin zone for various values of q_z.

$q_\parallel$ changes from Γ to X the plasmon peak disperses to higher energies eventually entering the particle-hole continuum around $(\pi/2, 0)$, where the peak intensity sharply decreases. As q_z increases the plasmon energy at Γ decreases, becoming zero for $q_z > 0.04$. Moreover, the plasmon dispersion along $\Gamma - X$ softens becoming linear for $q_z > 0.3$, ultimately merging with the electron-hole continuum for very large q_z, which dampens out the plasmon peak entirely. The evolution of the plasmon with q_z is in agreement with Ref. [59]. Figure 5(c) compare the measured acoustic-plasmon energy with that from the calculated loss function plotted in Fig. 4 for $q_\parallel = 0.1$. The calculations further verify the decreased plasmon energy as being due to the increase of q_z and reveal the plasmon origin of the observed RIXS excitation.

E. Analysis of spectral weights

In combination with the absence of acoustic plasmon in Cu L-edge RIXS measurements[9–14], the results of O K-edge RIXS tuned to the ZRS resonance seem to suggest that the acoustic plasmons are predominantly of a O $2p$ character[25]. This conclusion, however, is in contrast to the ZRS picture[29], in which O $2p$ and Cu $3d$ are strongly hybridized and the singlet hops through the

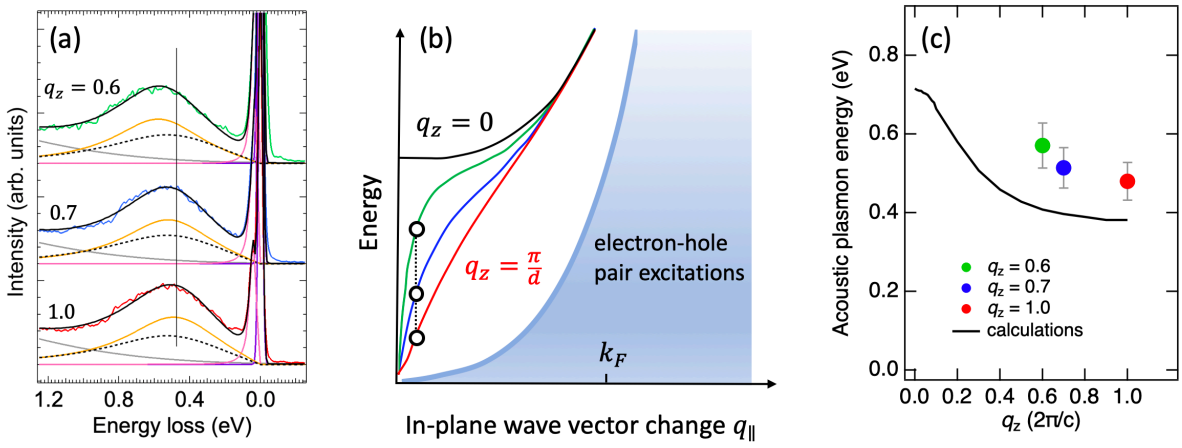

FIG. 5. 3D nature of acoustic plasmons. (a) RIXS spectra of LSCO after data smoothing for selected q_z with $q_\parallel$ fixed to 0.1. The incident X-ray energy was tuned to the ZRS resonance. The fitted spectral function for the plasmon and bimagnon is the anti-symmetrized Lorentzian function, as plotted in orange curves and black dashed lines, respectively; the background curves are plotted in grey lines. Bimagnon spectra of all q_z have the same energy position and width. Spectra are vertically offset for clarity. The vertical line indicates the plasmon energy of $q_z = 1.0$. See Supplemental Material[55] for the details of curve fitting. (b) Graphic illustration of the dispersion relations of selected plasmon bands and the electron-hole pair excitations of a layered electron-gas model (after Ref. [7]). The circles indicate the plasmon energy in response to the change in q_z with $q_\parallel$ fixed. (c) Comparison of the measured acoustic plasmon energies with those from the calculated loss function for $q_\parallel = 0.1$. The measured plasmon energies plotted as colored circles correspond to spectra shown in (a), from which the plasmon energies were deduced through curve fitting. The plasmon energy plotted by the black line is from the calculated loss function shown in Fig. 4.

Cu^{2+} lattice in a way similar to a hole in the single-band effective Hamiltonian. In hole-doped cuprates, the ZRS band crosses the Fermi level at wave vectors near $(\pi, 0)$ and $(\frac{\pi}{2}, \frac{\pi}{2})$, as shown in angle-resolved photoemission measurements[61,62]. One can use a simple cluster model[63] to comprehend the spectral weight of the transitions from the ground state to the unoccupied ZRS and UHB probed by O K-edge RIXS; the former has a comparable spectral weight of O $2p$ and Cu $3d$ orbitals, whereas the latter is dominated by Cu $3d$.

In O K-edge RIXS, the O $1s$ electron is excited to the ZRS or UHB. Theoretically, one can use a model Hamiltonian and the Kramers-Heisenberg formula to calculate RIXS cross section[64]. To comprehend the spectral weight of a RIXS process, we approximate the excitation as a transition from the ground state to an excited state. We used a simple cluster model[63] to obtain the spectral weight. In the following approximation, we neglect the effect of core hole in the intermediate state. For a cluster model, the state of a Cu^{2+} ion surrounded by four oxygens is described as

$$|\psi_{Cu^{2+}}\rangle = \alpha\,|d^9\rangle + \beta\,|d^{10}\underline{L}\rangle\,, \tag{7}$$

and the ZRS and UHB states are

$$|\mathrm{ZRS}\rangle = \gamma\,|d^8\rangle + \delta\,|d^9\underline{L}\rangle + \epsilon\,|d^{10}\underline{L}^2\rangle \tag{8}$$

$$|\mathrm{UHB}\rangle = |d^{10}\rangle\,, \tag{9}$$

where $\underline{L}$ represents a ligand hole. The RIXS cross section at the ZRS and UHB resonances are approximately proportional to $|\langle\psi_{Cu^{2+}}|\,\hat{a}_i^\dagger\,|\mathrm{ZRS}\rangle|^2$ and $\left|\langle\mathrm{UHB}|\,\hat{a}_i^\dagger\,|\psi_{Cu^{2+}}\rangle\right|^2$ (i = Cu $3d$, O $2p$), respectively, where $\hat{a}_i^\dagger$ is the electron creation operator on orbital i. We extract the spectral weights of O $2p$ and Cu $3d$ at the ZRS resonance as follows:

$$I_{\mathrm{ZRS}}^{O2p} = |\alpha\delta + \beta\epsilon|^2 \tag{10}$$

and

$$I_{\mathrm{ZRS}}^{Cu3d} = |\alpha\gamma + \beta\delta|^2\,. \tag{11}$$

Similarly, the spectral weights of O $2p$ and Cu $3d$ at the UHB resonance are:

$$I_{\mathrm{UHB}}^{O2p} = |\beta|^2 \tag{12}$$

$$I_{\mathrm{UHB}}^{Cu3d} = |\alpha|^2\,. \tag{13}$$

From the coefficients given by Eskes et al. for CuO (Ref. [63]), we have $\alpha = \sqrt{0.67}$, $\beta = \sqrt{0.33}$, $\gamma = \sqrt{0.07}$, $\delta = \sqrt{0.64}$ and $\epsilon = \sqrt{0.28}$. This gives $I_{\mathrm{ZRS}}^{O2p} = 0.86$, $I_{\mathrm{ZRS}}^{Cu3d} = 0.43$, $I_{\mathrm{UHB}}^{O2p} = 0.33$ and $I_{\mathrm{UHB}}^{Cu3d} = 0.67$. Therefore, O $2p$ and Cu $3d$ orbitals have a comparable spectral weight in the RIXS transition at the ZRS resonance, whereas the transition to the UHB is dominated by Cu $3d$. (Note: That $I_{\mathrm{ZRS}}^{O2p} + I_{\mathrm{ZRS}}^{Cu3d}$ exceeds 1 is due to the so-called "dynamical effect" of spectral weight transfer widely seen in correlated systems.) Calculations using the three-orbital Hubbard model[34] for hole-doped cuprates also indicate that the spectral weight of Cu $3d_{x^2-y^2}$ in the ZRS band is comparable to that of O $2p$ and that in the UHB band is dominated by Cu $3d_{x^2-y^2}$. Our observation of plasmons at both ZRS and UHB resonances unravels that

the acoustic plasmons are of ZRS character, consistent with the delocalized nature of the ZRS. In other words, not only O $2p$ but also Cu $3d$ states contribute to the itinerant motion of charge carriers in hole-doped cuprates.

IV. CONCLUSIONS

In conclusion, our observation of acoustic plasmons sheds light on the nature of the conducting carriers of hole-doped cuprates. O K-edge RIXS results demonstrate that the p and d orbitals are hybridized in ZRS bands and UHB, consistent with XAS results. The observation of plasmons at both UHB and ZRS resonances corroborates the ZRS picture, revealing that the acoustic plasmons indeed result from the delocalized nature of the ZRS. Our findings indicate that the conducting carriers are ZRS rather than O $2p$ holes.

Acknowledgements

We acknowledge NSRRC staff for technical support. We thank Teppei Yoshida for his technical advice on cleaving LSCO crystals. This work was supported in part by the Ministry of Science and Technology of Taiwan under Grant No. 103-2112-M-213-008-MY3 and MOST 108-2923-M-213-001. We acknowledge the support of Japan Society for the Promotion of Science under Grant No. 19K03741. The work at Northeastern University was supported by the US Department of Energy (DOE), Office of Science, Basic Energy Sciences grant number DE-FG02-07ER46352 and benefited from Northeastern University's Advanced Scientific Computation Center (ASCC), and the NERSC supercomputing center through DOE grant number DE-AC02-05CH11231. The work at Los Alamos National Laboratory was supported by the U.S. DOE NNSA under Contract No. 89233218CNA000001 and the Center for Integrated Nanotechnologies, a DOE BES user facility in partnership with the LANL Institutional Computing Program for computational resources. Additional support was provided by DOE Office of Basic Energy Sciences Program E3B5.

* Corresponding author: djhuang@nsrrc.org.tw

[1] B. Keimer, S. A. Kivelson, M. R. Norman, S. Uchida, and J. Zaanen, Nature **518**, 179 (2015).
[2] M. Imada, A. Fujimori, and Y. Tokura, Rev. Mod. Phys. **70**, 1039 (1998).
[3] K. Segawa, M. Kofu, S. Lee, I. Tsukada, H. Hiraka, M. Fujita, S. Chang, K. Yamada, and Y. Ando, Nat. Phys. **6**, 579 (2010).
[4] C. Weber, K. Haule, and G. Kotliar, Nat. Phys. **6**, 574 (2010).
[5] M. Hepting, L. Chaix, E. W. Huang, R. Fumagalli, Y. Y. Peng, B. Moritz, K. Kummer, N. B. Brookes, W. C. Lee, M. Hashimoto, T. Sarkar, J. F. He, C. R. Rotundu, Y. S. Lee, R. L. Greene, L. Braicovich, G. Ghiringhelli, Z. X. Shen, T. P. Devereaux, and W. S. Lee, Nature **563**, 374 (2018).
[6] J. Lin, J. Yuan, K. Jin, Z. Yin, G. Li, K.-J. Zhou, X. Lu, M. Dantz, T. Schmitt, H. Ding, D. M. P. M. Guo, Haizhong, and X. Liu, npj Quantum Mater. **5**, 1 (2020).
[7] V. Z. Kresin and H. Morawitz, Phys. Rev. B **37**, 7854 (1988).
[8] A. Greco, H. Yamase, and M. Bejas, Commun. Phys. **2**, 3 (2019).
[9] L. Braicovich, J. Van den Brink, V. Bisogni, M. M. Sala, L. Ament, N. Brookes, G. De Luca, M. Salluzzo, T. Schmitt, V. Strocov, *et al.*, Phys. Rev. Lett. **104**, 077002 (2010).
[10] M. Le Tacon, G. Ghiringhelli, J. Chaloupka, M. M. Sala, V. Hinkov, M. Haverkort, M. Minola, M. Bakr, K. Zhou, S. Blanco-Canosa, *et al.*, Nat. Phys. **7**, 725 (2011).
[11] M. Dean, A. James, R. Springell, X. Liu, C. Monney, K. Zhou, R. Konik, J. Wen, Z. Xu, G. Gu, *et al.*, Phys. Rev. Lett. **110**, 147001 (2013).
[12] M. Minola, G. Dellea, H. Gretarsson, Y. Peng, Y. Lu, J. Porras, T. Loew, F. Yakhou, N. Brookes, Y. Huang, *et al.*, Phys. Rev. Lett. **114**, 217003 (2015).
[13] M. Minola, Y. Lu, Y. Peng, G. Dellea, H. Gretarsson, M. Haverkort, Y. Ding, X. Sun, X. Zhou, D. Peets, *et al.*, Phys. Rev. Lett. **119**, 097001 (2017).
[14] K. Ishii, T. Tohyama, S. Asano, K. Sato, M. Fujita, S. Wakimoto, K. Tustsui, S. Sota, J. Miyawaki, H. Niwa, *et al.*, Phys. Rev. B **96**, 115148 (2017).
[15] N. Nücker, U. Eckern, J. Fink, and P. Müller, Phys. Rev. B **44**, 7155 (1991).
[16] J. Fink, M. Knupfer, S. Atzkern, and M. S. Golden, J. Electron. Spectrosc. Relat. Phenom. **117**, 287 (2001).
[17] F. Roth, A. König, J. Fink, B. Büchner, and M. Knupfer, J. Electron. Spectrosc. Relat. Phenom. **195**, 85 (2014).
[18] M. Mitrano, A. A. Husain, S. Vig, A. Kogar, M. S. Rak, S. I. Rubeck, J. Schmalian, B. Uchoa, J. Schneeloch, R. Zhong, G. D. Gu, and P. Abbamonte, Proc. Natl. Acad. Sci. U.S.A. **115**, 5392 (2018).
[19] A. A. Husain, M. Mitrano, M. S. Rak, S. Rubeck, B. Uchoa, K. March, C. Dwyer, J. Schneeloch, R. Zhong, G. D. Gu, and P. Abbamonte, Phys. Rev. X **9**, 041062 (2019).
[20] I. Bozovic, Phys. Rev. B **42**, 1969 (1990).
[21] S. Uchida, T. Ido, H. Takagi, T. Arima, Y. Tokura, and S. Tajima, Phys. Rev. B **43**, 7942 (1991).
[22] D. van der Marel, J. Supercond. **17**, 559 (2004).
[23] J. Levallois, M. K. Tran, D. Pouliot, C. N. Presura, L. H. Greene, J. N. Eckstein, J. Uccelli, E. Giannini, G. D. Gu, A. J. Leggett, and D. van der Marel, Phys. Rev. X **6**, 031027 (2016).
[24] X. Yin, C. S. Tang, S. Zeng, T. C. Asmara, P. Yang, M. A. Naradipa, P. E. Trevisanutto, T. Shirakawa, B. H. Kim, S. Yunoki, *et al.*, ACS Photonics **6**, 3281 (2019).
[25] A. Nag, M. Zhu, M. Bejas, J. Li, H. C. Robarts, H. Yamase,

A. N. Petsch, D. Song, H. Eisaki, A. C. Walters, M. García-Fernández, A. Greco, S. M. Hayden, and K.-J. Zhou, Phys. Rev. Lett. **125**, 257002 (2020).
[26] S. Ono, S. Komiya, and Y. Ando, Phys. Rev. B **75**, 024515 (2007).
[27] A. Fujimori, E. Takayama-Muromachi, Y. Uchida, and B. Okai, Phys. Rev. B **35**, 8814 (1987).
[28] V. Emery, Phys. Rev. Lett. **58**, 2794 (1987).
[29] F. C. Zhang and T. M. Rice, Phys. Rev. B **37**, 3759 (1988).
[30] C. T. Chen, F. Sette, Y. Ma, M. S. Hybertsen, E. B. Stechel, W. M. C. Foulkes, M. Schulter, S.-W. Cheong, A. S. Cooper, L. W. Rupp Jr, *et al.*, Phys. Rev. Lett. **66**, 104 (1991).
[31] P. Abbamonte, L. Venema, A. Rusydi, G. Sawatzky, G. Logvenov, and I. Bozovic, Science **297**, 581 (2002).
[32] L. Tjeng, C. Chen, and S.-W. Cheong, Phys. Rev. B **45**, 8205 (1992).
[33] M. Hashimoto, I. M. Vishik, R.-H. He, T. P. Devereaux, and Z.-X. Shen, Nat. Phys. **10**, 483 (2014).
[34] C.-C. Chen, M. Sentef, Y. F. Kung, C. J. Jia, R. Thomale, B. Moritz, A. P. Kampf, and T. P. Devereaux, Phys. Rev. B **87**, 165144 (2013).
[35] S. Komiya, Y. Ando, X. F. Sun, and A. N. Lavrov, Phys. Rev. B **65**, 214535 (2002).
[36] S. Komiya, H.-D. Chen, S.-C. Zhang, and Y. Ando, Phys. Rev. Lett. **94**, 207004 (2005).
[37] H. Kanai, J. Mizusaki, H. Tagawa, S. Hoshiyama, K. Hirano, K. Fujita, M. Tezuka, and T. Hashimoto, J. Solid State Chem. **131**, 150 (1997).
[38] H. Takagi, T. Ido, S. Ishibashi, M. Uota, S. Uchida, and Y. Tokura, Phys. Rev. B **40**, 2254 (1989).
[39] A. Singh, H. Huang, Y. Chu, C. Hua, S. Lin, H. Fung, H. Shiu, J. Chang, J. Li, J. Okamoto, *et al.*, J. Synchrotron Radiat. **28**, 977 (2021).
[40] C. T. Chen, L. H. Tjeng, J. Kwo, H. L. Kao, P. Rudolf, F. Sette, and R. M. Fleming, Phys. Rev. Lett. **68**, 2543 (1992).
[41] T. Nomura and J. Igarashi, Phys. Rev. B **71**, 035110 (2005).
[42] R. Markiewicz and A. Bansil, Phys. Rev. Lett. **96**, 107005 (2006).
[43] R. Markiewicz, M. Hasan, and A. Bansil, Phys. Rev. B **77**, 094518 (2008).
[44] K. Sturm, Z. Naturforsch. **48a**, 233 (2013).
[45] F. Aryasetiawan and S. Biermann, Phys. Rev. Lett. **100**, 116402 (2008).
[46] S. Sahrakorpi, R. S. Markiewicz, H. Lin, M. Lindroos, X. J. Zhou, T. Yoshida, W. L. Yang, T. Kakeshita, H. Eisaki, S. Uchida, S. Komiya, Y. Ando, F. Zhou, Z. X. Zhao, T. Sasagawa, A. Fujimori, Z. Hussain, Z.-X. Shen, and A. Bansil, Phys. Rev. B **78**, 104513 (2008).
[47] C. Lane, Phys. Rev. B **101**, 235138 (2008).
[48] R. Markiewicz, S. Sahrakorpi, M. Lindroos, H. Lin, and A. Bansil, Phys. Rev. B **72**, 054519 (2005).
[49] R. Markiewicz, I. Buda, P. Mistark, C. Lane, and A. Bansil, Sci. Rep. **7**, 44008 (2017).
[50] R. S. Markiewicz and A. Bansil, Phys. Rev. B **75**, 020508 (2007).
[51] C. Lane, J. W. Furness, I. G. Buda, Y. Zhang, R. S. Markiewicz, B. Barbiellini, J. Sun, and A. Bansil, Phys. Rev. B **98**, 125140 (2018).
[52] J. W. Furness, Y. Zhang, C. Lane, I. G. Buda, B. Barbiellini, R. S. Markiewicz, A. Bansil, and J. Sun, Commun. Phys. **1**, 11 (2018).
[53] H. Y. Huang, A. Singh, C. Y. Mou, S. Johnston, A. F. Kemper, J. van den Brink, P. J. Chen, T. K. Lee, J. Okamoto, Y. Y. Chu, J. H. Li, S. Komiya, A. C. Komarek, A. Fujimori, C. T. Chen, and D. J. Huang, Phys. Rev. X **11**, 041038 (2021).
[54] V. Bisogni, M. Moretti Sala, A. Bendounan, N. B. Brookes, G. Ghiringhelli, and L. Braicovich, Phys. Rev. B **85**, 214528 (2012).
[55] See Supplemental Material at [URL will be inserted by publisher] for further information about RIXS curve fitting and calculations of the dielectric function.
[56] L. Chaix, E. W. Huang, S. Gerber, X. Lu, C. Jia, Y. Huang, D. E. McNally, Y. Wang, F. H. Vernay, A. Keren, M. Shi, B. Moritz, Z.-X. Shen, T. Schmitt, T. P. Devereaux, and W.-S. Lee, Phys. Rev. B **97**, 155144 (2018).
[57] A. Achkar, T. Regier, H. Wadati, Y.-J. Kim, H. Zhang, and D. Hawthorn, Phys. Rev. B **83**, 081106 (2011).
[58] B. Kyung, V. Hankevych, A.-M. Daré, and A.-M. S. Tremblay, Phys. Rev. Lett. **93**, 147004 (2004).
[59] V. Kresin and H. Morawitz, Phys. Rev. B **37**, 7854 (1988).
[60] A. Greco, H. Yamase, and M. Bejas, Phys. Rev. B **94**, 075139 (2016).
[61] T. Yoshida, X. J. Zhou, T. Sasagawa, W. L. Yang, P. V. Bogdanov, A. Lanzara, Z. Hussain, T. Mizokawa, A. Fujimori, H. Eisaki, Z.-X. Shen, T. Kakeshita, and S. Uchida, Phys. Rev. Lett. **91**, 027001 (2003).
[62] K. M. Shen, F. Ronning, D. H. Lu, W. S. Lee, N. J. C. Ingle, W. Meevasana, F. Baumberger, A. Damascelli, N. P. Armitage, L. L. Miller, Y. Kohsaka, M. Azuma, M. Takano, H. Takagi, and Z.-X. Shen, Phys. Rev. Lett. **93**, 267002 (2004).
[63] H. Eskes, L. H. Tjeng, and G. A. Sawatzky, Phys. Rev. B **41**, 288 (1990).
[64] L. J. P. Ament, M. van Veenendaal, T. P. Devereaux, J. P. Hill, and J. van den Brink, Rev. Mod. Phys. **83**, 705 (2011).
[65] C. Lane and J.-X. Zhu, Phy. Rev. B **101**, 155135 (2020).
[66] T. Das, R. Markiewicz, and A. Bansil, Phys. Rev. B **81**, 174504 (2010).
[67] E. Collart, A. Shukla, J.-P. Rueff, P. Leininger, H. Ishii, I. Jarrige, Y. Q. Cai, S.-W. Cheong, and G. Dhalenne, Phys. Rev. Lett. **96**, 157004 (2006)
.